An analytical method to predict and compensate for residual stress-induced deformation in overhanging regions of internal channels fabricated using powder bed fusion

Kamat, Amar M.; Pei, Yutao T.

Published in:
Additive Manufacturing

DOI:
10.1016/j.addma.2019.100796

Publication date:
2019

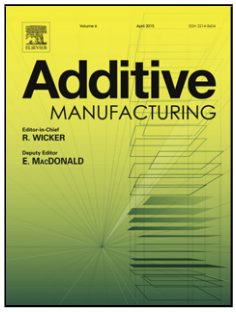

Title: An analytical method to predict and compensate for residual stress-induced deformation in overhanging regions of internal channels fabricated using powder bed fusion

Authors: Amar M. Kamat, Yutao Pei

PII: S2214-8604(19)30346-X
DOI: https://doi.org/10.1016/j.addma.2019.100796
Article Number: 100796

Reference: ADDMA 100796

To appear in:

Received date: 24 March 2019
Revised date: 5 June 2019
Accepted date: 16 July 2019

Please cite this article as: Kamat AM, Pei Y, An analytical method to predict and compensate for residual stress-induced deformation in overhanging regions of internal channels fabricated using powder bed fusion, *Additive Manufacturing* (2019), https://doi.org/10.1016/j.addma.2019.100796

An analytical method to predict and compensate for residual stress-induced deformation in overhanging regions of internal channels fabricated using powder bed fusion

Amar M. Kamat, Yutao Pei*

Advanced Production Engineering, Engineering and Technology Institute Groningen, Faculty of Science and Engineering, University of Groningen, Nijenborgh 4, 9747 AG Groningen, the Netherlands

* Corresponding author, e-mail: y.pei@rug.nl

Abstract

Powder bed fusion (PBF) is ideally suited to build complex and near-net-shaped metallic structures such as conformal cooling channel networks in injection molds. However, warpage occurring due to the residual stresses inherent to this process can lead to shape deviation in the internal channels and needs to be minimized. In this research, a novel analytical model based on the Euler-Bernoulli beam bending theory was developed to estimate the residual stress-induced deformation of internal channels printed horizontally using PBF. The model was used to predict the shape deviation for three different shapes of channel cross sections (circular, elliptical, and diamond-shaped), and showed very good agreement with the experimentally determined shapes of nine different internal channels (three cases per cross-sectional shape). Further, the model predictions were used to compensate for the shape deviation in the design stage, resulting in a reduction in root mean square (RMS) deviation of the circular channel by a factor of 2. The proposed approach is thus expected to be a useful

tool to generate design-for-AM guidelines for the additive manufacturing of overhangs and internal channels.

Keywords: Powder bed fusion; Selective laser melting; Internal channels; Residual stresses; Overhang; Shape compensation; 17-4 PH stainless steel

1. Introduction

Powder bed fusion (PBF) is a type of metal additive manufacturing (AM) process in which thermal energy (usually a focused laser beam) selectively fuses regions of a metal powder bed to build up a three-dimensional (3D) metallic part layer-by-layer [1,2]. Due to its ability to create complex and (near-)net-shape metallic parts with high relative densities (up to 99.8 % [3,4]) and mechanical properties comparable or better than their wrought counterparts [5], PBF is one of the preferred metal AM processes to realize complicated designs that were previously impossible to fabricate using conventional manufacturing techniques. For instance, PBF has been used to create patient-specific implants [6], dental prostheses [4], 3D cellular lattice structures [7] that can be used to make lightweight components [8], topology-optimized structures with applications in the biomedical [9] and aerospace industries [10], intricate cooling channel networks in gas turbines [11] and injection molds [12,13], and so on, thus enabling customization and long-term cost savings [14]. In spite of the greater design freedom offered by the PBF process, this processing technique is still beset by challenges such as expensive raw material (i.e. spherical gas-atomized metal powder), limitations on part size, part defects such as porosity and cracks, surface roughness, anisotropy in static and dynamic properties, slow build rates, and residual stresses [15]. A schematic of the PBF process is shown in Fig. 1 [16].

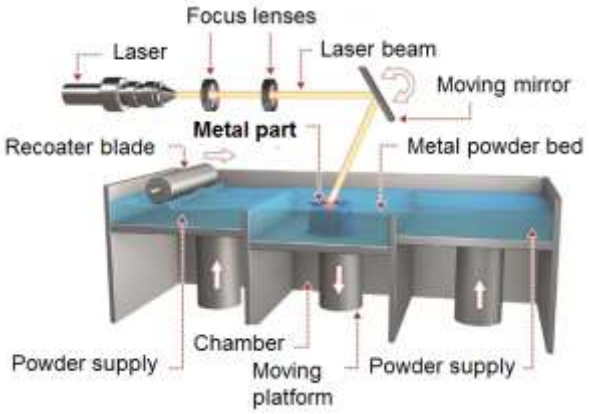

Fig. 1. Schematic of the laser powder bed fusion (PBF) process (adapted from Ref. [16]).

Residual stresses are defined as internal stresses in a body that is at equilibrium with its surroundings [17]. Mercelis *et al.* [18] described two mechanisms for the development of residual stresses in a PBF process, namely, the thermal gradient mechanism and the cool-down mechanism. The nature of the PBF process, wherein a moving energy source (usually a focused laser beam) melts and fuses metal powder into a densified part, gives rise to high thermal gradients in the vicinity of the melt pool. The heated region first experiences plastic compressive stresses during heat-up (when its expansion is resisted by the cooler neighboring regions causing the local strains to exceed the elastic compressive strain limit) followed by plastic tensile stresses during cool-down (when its shrinkage is again resisted by the neighboring regions causing the local strains to now exceed the elastic tensile strain limit). This sequence of events culminates in a residual tensile stress in the selectively laser-melted region according to the thermal gradient mechanism. When the deposited layer solidifies, its shrinkage is resisted by the underlying layers, causing a tensile stress in the deposited layer and compressive stresses in the underlying layers, according to the cool-down mechanism [18]. Spatial temperature gradients (large enough to cause an expansion mismatch between the heated region and its surroundings), thermal expansion coefficients (high enough to cause the thermal strains to exceed the elastic strain limit at typical temperatures reached in the PBF

process), and temperature-dependent flow stresses have been identified by Debroy *et al.* [5] as the key factors contributing to residual stresses in the PBF process. Residual stresses are undesirable because they can degrade the mechanical properties [5,18–20], induce cracks and delamination [21], and distort the PBF-built part which can lead to interference of the part with the recoater blade [22] and lower dimensional tolerances [23], thus necessitating a detailed understanding of the origin of residual stresses with a view to mitigating them. Several thermomechanical models exist in the literature that simulated the PBF process utilizing either analytical or finite element approaches; the general aim of these models has been to study the effects of processing parameters (laser power, scan speed, hatch spacing, powder layer thickness, build plate temperature, and so on), scan strategy ('stripe', 'island' or 'chess', 'meandering', and so on), and post-print heat treatment on the residual stress development and part distortion.

Matsumoto *et al.* [24] published one of the first finite element (FE) models to simulate multiple laser tracks comprising a single layer in the PBF process, and found that shorter scanning tracks led to lower residual stresses in the solidified material. Klingbeil *et al.* [25] developed 1-D and 2-D thermomechanical finite element (FE) models to estimate residual-stress induced warpage in two different metal deposition AM processes (termed as 'Shape Deposition Manufacturing' by the authors); these models were applicable for multiple rows comprising a single layer of metal deposited upon a substrate. They identified residual stress-induced warpage as the major obstacle to overcome in AM processes, and found that maximizing substrate preheating (through both external heating and optimized scan strategies) and mechanical constraints resulted in minimum warpage of the build plate; although different from the PBF processes, their insights were general enough to be applicable to all laser-based AM processes. Shiomi *et al.* [26] and Mercelis *et al.* [18] developed experimentally validated analytical models of the residual stress development in

the PBF process, taking into account the layer-by-layer nature of the printing process; both authors assumed the last deposited layer to be in a state of tensile residual stress equal to the yield strength of the material, and were able to derive expressions for the residual stress profile along the depth of the printed part and the build plate. Shiomi *et al.* [26] recommended heat treatment to reduce residual stresses, while Mercelis *et al.* [18] advocated optimized laser scan strategies for the same. Mercelis *et al.* [18] further observed that the residual stress profiles reduced drastically after the part was removed from the build plate due to relaxation stresses, which led to uniform shrinkage and bending deformation of the removed part. Subsequently, several researchers developed three-dimensional (3D) thermomechanical analytical [27] and FE [28–31] models that were able to simulate individual laser tracks for multiple layers; these models recognized the anisotropy in the stress profiles (e.g. residual stress parallel to the scan vector was greater than the stress perpendicular to the scan vector [27,30]) and the importance of controlling temperature gradients (through optimized processing parameters [28,31], scan strategies [29,30], and substrate preheating [28]) to minimize residual stresses. Although these models shed considerable light on the physics of the PBF process, they were computationally expensive and allowed only a maximum of up to three layers to be modeled. Consequently, several coarse-grained thermomechanical FE approaches [32–36] were developed that either modeled the deposition of entire layers at once [32,33,36] or considered equivalent heat sources to mimic the effect of multiple successive laser scan vectors [34,35]; while these models could not simulate the effect of laser scan strategy explicitly and combined multiple layers together for computational efficiency, they were practical enough to estimate residual stresses and distortions in real parts, allowing convenient experimental validation via, for instance, distortion of cantilever beams (after support removal) built using PBF. The utility of using such mesoscale model predictions for creating compensation models to minimize

distortions in PBF-built industrial components was recently demonstrated by Azafov *et al.* [23,37].

Residual stress-induced deformation is especially severe for overhanging regions which, by definition, are printed without any support structures beneath them. Usually, this problem is addressed by building the overhanging regions on support structures that can later be machined away; however, this is always undesirable (due to additional post-processing, material costs and potential damage to the part) and often difficult (e.g. in internal cooling channel applications where support removal is impossible due to lack of accessibility). Understanding the shape deviation in overhanging features during the PBF process, with a view to predicting it and ultimately developing generalized design rules, is thus an important challenge that has been the focus of recent research [38]; however, the application of the analytical and FE models described earlier to predict distortion of overhanging features has been limited, and the studies on overhang shape deviation have primarily been experimental in nature. In his PhD dissertation, Thomas [39] performed a comprehensive set of experiments on 316L stainless steel to develop design rules for the PBF process; using a qualitative scoring system for residual-stress induced curl in overhanging features (0-3 where 0 represented no curl and 3 represented serious curl that caused build failure due to recoater-part collision), he identified a critical overhang angle (with respect to the build direction) of 45° for linear overhanging shapes above which unacceptable shape deviation or build failure was expected to occur. For non-linear overhanging shapes, such as concave or convex radii used in chamfers and fillets, Thomas [39] suggested that the residual stress-induced curl was proportional to the number of layers that had an overhang angle greater than 45°; further, he found that horizontally printed circular holes above a diameter of 7 mm curled excessively at the top and had to be built with supports or redesigned into a self-supporting profile. Kranz *et al.* [40] developed design guidelines for lightweight structures made out of the Ti-6Al-4V

alloy, and recommended the use of support structures for a critical angle greater than 50°, and for horizontal holes of diameter greater than 12 mm to avoid curling. Wang *et al.* [41] conducted experiments on 316L stainless steel and argued that to minimize the degree of curling, the local overhanging length (equal to $t \times \tan\theta$ where t is the layer thickness and θ is the overhang angle measured with respect to the build direction) should be less than the beam radius; based on a beam diameter of 70 μm and a layer thickness of 35 μm, they calculated this critical angle to be 45° in agreement with Thomas [39]. Wang *et al.* [41] also found that higher energy density (e.g. caused by high laser power and/or low scan speed) caused greater warpage in overhanging regions, and advocated the use of a lower energy density while scanning critical areas of the overhanging regions. Wang *et al.* [41,42] further noted the cumulative effect of warpage caused by the melting and solidification of successive layers in the PBF process. Cheng *et al.* [43] created a two-dimensional (2D) FE model to compare the residual stresses and distortions in an overhanging layer with those in a layer built over a solid substrate, and found that the overhanging region exhibited lower residual stresses and higher distortions; moreover, they found an approximately linear relationship between energy density and residual stress-induced distortion overhanging regions, confirming the experimental findings of Wang *et al.* [41,42]. Calignano [44] built overhanging structures such as concave and convex radii with Ti-6Al-4V and Al-Si10-Mg alloys, and recommended anchoring the overhanging region using optimized support structures to reduce warpage. Mertens *et al.* [45] built linear overhangs (angles 30°, 45°, and 60° with respect to the build direction) with the Al-Si10-Mg alloy, and found that thermal stresses induced a warp of up to 1.5° for the extreme case (60° overhang angle) even with an optimized scan strategy.

The problem of predicting distortion is especially important in internal cooling channels, where anchoring the overhanging regions with support structures is undesirable due to the

difficulty in removing the support structures after the build is complete. In addition to residual stress-induced deformation, partial sintering of powder particles on the inner walls of overhanging regions can also increase the surface roughness of internal channels, lowering their dimensional accuracy due to dross formation [46,47]. In general, the surface quality of PBF-built parts depends on the powder characteristics, with finer powder sizes and wider powder size distributions deemed beneficial for reducing surface roughness [48]. The shape deviation in internal channels is most critical when the channels are built horizontally (i.e. when the channel axis is perpendicular to the build direction) due to large overhanging areas near the top of the channels, making them susceptible to residual stress-induced curling and dross formation [47,49,50]. Fig. 2a shows an example of a horizontally printed circular channel divided into three regions based on the tendency to warp [41]: region I is built upon previously solidified material and hence does not have any overhanging areas; region II has overhanging areas with low enough overhanging angles to not show any appreciable warpage or dross formation; finally, region III has high overhanging angles that need counteractive measures to maintain tight tolerances. Researchers have tried to minimize the shape deviation of region III either by using a reduced local energy density when scanning these regions [41,45] or by redesigning the shape of region III into a self-supporting 'teardrop' profile [39,46,49,51] as shown in Fig. 2b. However, the former approach can introduce local porosity due to incomplete fusion caused by the lowered energy density, while the latter approach can introduce stress concentration sites at the top of the teardrop profile which is detrimental to the fatigue life of the component. Shape compensation, whereby the pre-print design of the channel is modified to account for the expected distortion so that the printed shape will conform to the desired profile [44], is a potential solution to maintain the desired tolerances without encountering the above difficulties. In this work, an analytical methodology was formulated to predict the residual stress-induced shape deviation of the

overhanging regions in PBF-built internal channels. Treating the overhanging region as a cantilever of variable thickness and using classical Euler-Bernoulli beam bending theory, a second-order ordinary differential equation was derived that can be easily solved to obtain the shape deviation of any given channel shape. The model predictions were compared with experimental shape deviation observations for a total of nine cases (three different channel profiles -- circular, elliptical, and diamond-shaped), and very good agreement was observed. Finally, the utility of this approach to create a compensation model that successfully reduced the root mean square (RMS) deviation of a circular internal channel was demonstrated.

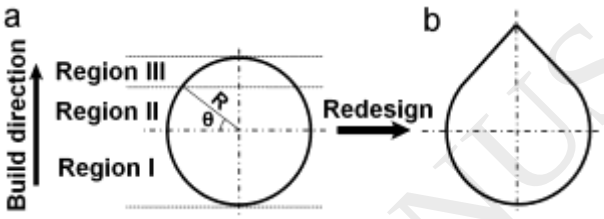

Fig. 2. Schematic of (a) horizontal circular channel divided into three regions based on their propensity to undergo warpage (terminology due to Wang *et al*. [41]), and (b) redesigned 'teardrop' shape where Region III is redesigned into a self-supporting linear shape.

2. Materials and methods

2.1 Powder bed fusion of 17-4 PH stainless steel

17-4 precipitation hardening (PH) stainless steel powder (LPW Technology, UK) was used in this study (Fig. 3). The powder was gas-atomized in argon and had a size distribution of 10-45 μm with an elemental composition shown in Table 1 (data obtained from supplier certificate).

Table 1
Elemental composition of 17-4 PH stainless steel powder (data from the powder supplier).

Element	C	Cr	Cu	Fe	Mn	Mo	N	Nb+Ta	Ni	O	P	S	Si
Wt. %	0.01	15.6	3.89	Bal.	0.24	<0.01	0.01	0.33	4.03	0.05	0.004	0.003	0.29

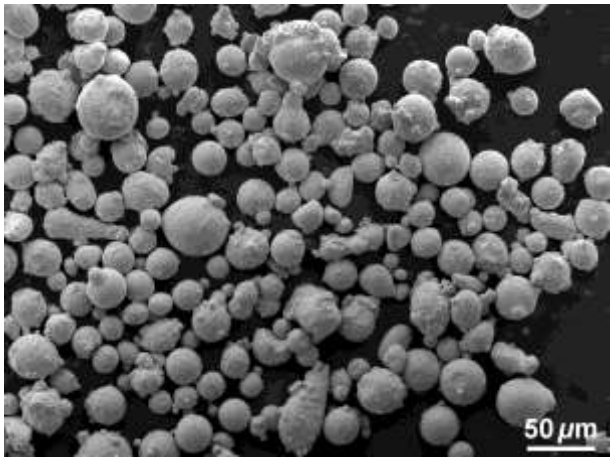

Fig. 3. SEM image of 17-4 PH powder particles.

The PBF experiments were performed using an SLM 125^{HL} machine (SLM Solutions, Germany). Manufacturer-recommended processing parameters, optimized to obtain high-density parts, were used in all the experiments; these parameters were also independently verified by building cubes (10 mm × 10 mm × 10 mm) using the same parameters, where high densities in excess of 99.8 % (measured via metallography and image processing) were observed. Relevant processing parameters and details about the SLM 125^{HL} machine are given in Table 2 and a schematic explaining the scan strategy and terminology is shown in Fig. 4. It should be noted that different processing parameters (resulting in a lowered energy density) were used while scanning overhanging regions to minimize the roughness of the underside of the overhanging regions, where the critical angle to define an overhanging region was set to 31° per the recommendations of the manufacturer.

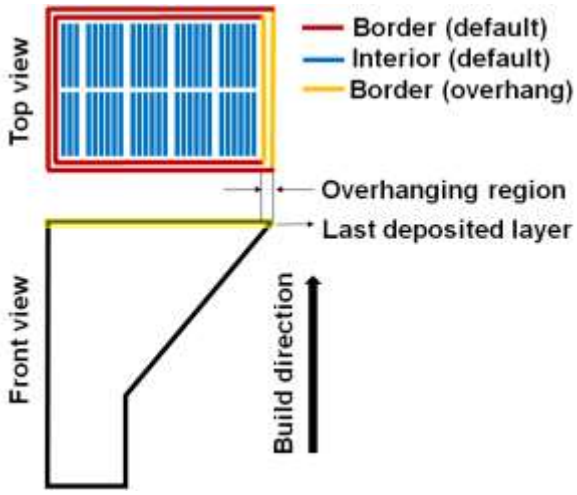

Fig. 4. Schematic showing the stripe scan strategy when scanning a layer involving an overhanging region. Each line in the top view represents a laser scan vector.

Table 2
Processing parameters and machine details.

	Default		Overhang	
Parameter	Interior	Border	Interior	Border
Laser power (W)	200	100	100	100
Scan speed (mm/s)	800	400	1000	1000
Hatch spacing (µm)	120	N/A	60	N/A
Layer thickness (µm)	30			
Build plate temperature (°C)	100			
Argon gas overpressure (mbar)	17			
Scan strategy	Stripes, 10 mm wide			
Hatch rotation angle	33° after every layer			
Laser beam details	1.07 µm wavelength, 70 µm spot size, Gaussian mode (M^2 ~ 1.19)			

To observe the shape deviation of internal channels built without support, a total of nine test coupons containing internal channels with overhanging regions were built using the above parameters for three different channel shapes – circular (diameter, D = 8, 10, 12 mm), elliptical (major axis = 6 mm, minor axis, b = 4, 4.5, and 5 mm), and diamond-shaped (angle with respect to vertical, $\varnothing$ = 40°, 45°, and 50°) – as shown in Figs. 5a-c. A photograph of three representative, as-built, test coupons attached to the build plate is shown in Fig. 5d. Since prior experiments showed considerable bending of the sides towards the hole for a channel-side distance of less than 7 mm, the hole was situated 10 mm away from the bottom

and side edges of the coupon (Figs. 5a-c) to prevent the deformation of the sides from affecting the shape deviation measurements of the internal holes. To observe the efficacy of pre-print compensation, the results of the shape deviation model (described in Section 3) were subtracted from the desired shape (a circle with D = 12 mm) to create a 'negative' deformation before the PBF build; three cases were studied: a horizontally built circle with shape compensation, a horizontally built circle without shape compensation (i.e. the same sample from the shape deviation experiments discussed before), and a vertically built circle as a reference. All the parts were secured on the build plate using block supports and were oriented such that the channel axis was horizontal and at an angle of 95° to the direction of recoater motion. It should be noted that the recoater blade was made of flexible rubber-like material, and hence collisions of warped regions with the recoater blade did not require the build job to be aborted, unless the warpage was severe, which was never the case in these experiments.

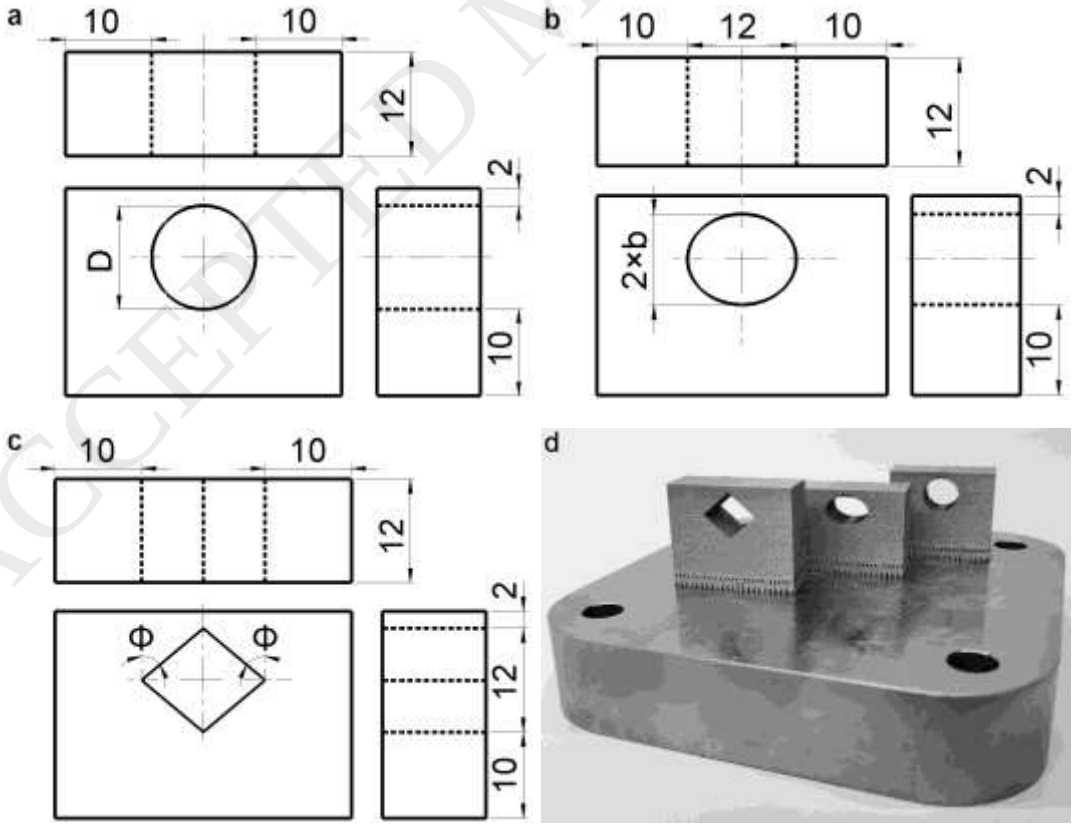

Fig. 5. Test coupons containing an internal hole of three different shapes for shape deviation experiments: (a) circular (D = 8, 10, and 12 mm), (b) elliptical (b = 4, 4.5, and 5 mm), and (c) diamond-shaped (Ø = 40°, 45°, and 50°). All dimensions in the drawings are in mm. (d) Photograph of three representative test coupons in the as-built condition.

2.2 Metallography and image processing

After the coupons were removed from the build plate, they were transversely sectioned through the middle portion of the channel length using a resin-bonded, abrasive, 1.5 mm thick blade (102508P, Buehler, USA) designed to cut stainless steels samples. The sectioning was conducted at a low cutting speed (approximately 0.04 mm/s) under continuous coolant flow to ensure minimal damage to the specimen. The cross-sections were then subjected to standard metallographic techniques of mounting, grinding, and polishing up to 1 µm diamond paste. Separate micrographs of different regions of the polished channel profiles were then obtained using an optical microscope (25× magnification) and manually stitched together (MS Paint) to get the micrograph of the complete channel. The stitched micrographs were processed using ImageJ [52] where they were converted to a binary image, following which the xy-coordinates of the channel profiles were extracted using the "wand" tracing tool of the software. To compare the acquired xy-coordinates of the PBF-built channels to the designed profile, a reference needed to be set: this was done by fitting the bottom half of the acquired xy-coordinates against the bottom half of the designed profiles – this was possible because the bottom half of the channels is expected to adhere to the design owing to a lack of overhanging regions. The image processing flow from stitched micrographs to the xy-coordinates for the case of diamond-shaped channel (Ø = 50°) is illustrated in Fig. 6.

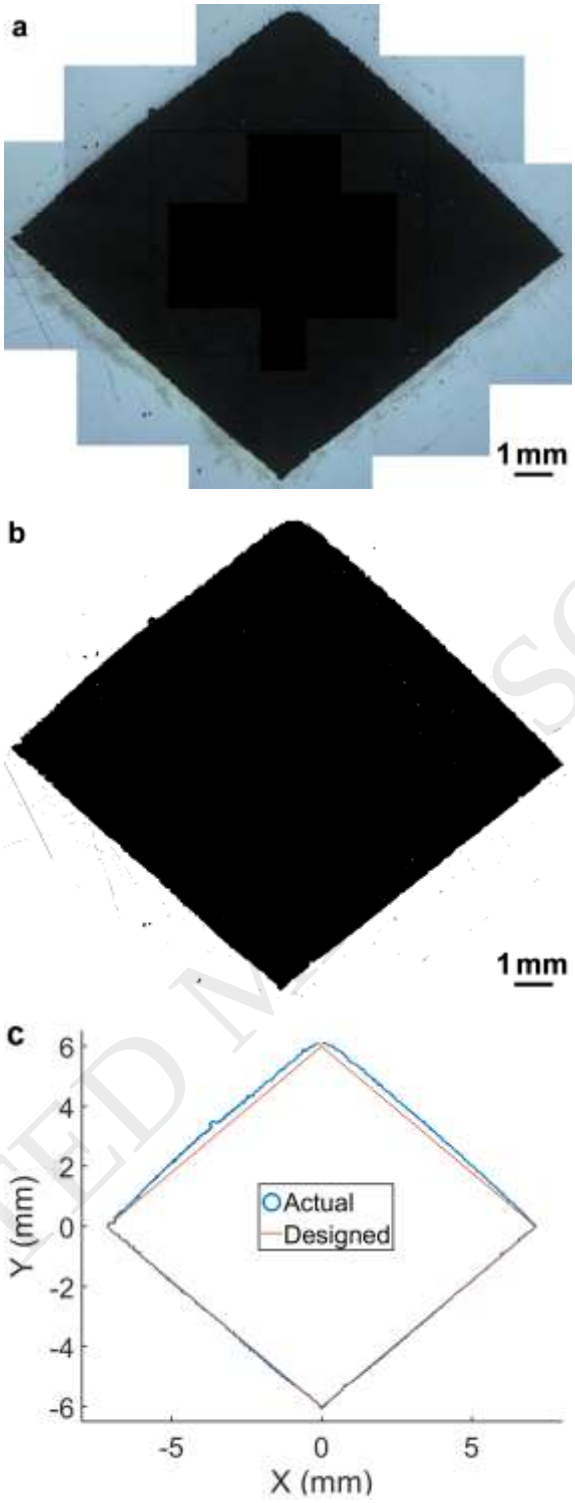

Fig. 6. Illustration of process flow to obtain xy-coordinates for one case (diamond-shaped channel, Ø=50°): (a) after stitching optical micrographs (25× magnification), (b) after converting stitched micrograph to a binary image in ImageJ, and (c) after extracting the xy-coordinates from the binary image and fitting the bottom half to the designed diamond-shape (Ø=50°).

2.3 Mechanical testing

Three 'plate-type' tensile test specimens conforming to the dimensions recommended by the ASTM E8/E8M standard [53] were built using PBF such that the tensile direction was parallel to the build plate and the specimen plane was perpendicular to the build plate. Care was taken while removing supports from underneath the gauge length to avoid introducing artificial notches in the specimen. The tensile tests were conducted on the MTS 810 universal testing machine and the yield strength was calculated using the 0.2 % strain offset method. Nanoindentation tests (MTS Nanoindenter XP) were conducted on the polished cross-sections of samples prepared for porosity measurements (see Section 2.1); sixteen indents were made on the transverse cross-section of the cube away from the edges under the force-controlled mode (maximum force = 40 mN). The Young's modulus of the sample was calculated from the instantaneous slope of the unloading point of the force-displacement curve [54]. Representative engineering stress-strain (tensile test) and force-displacement curves (nanoindentation) are shown in Fig. 7.

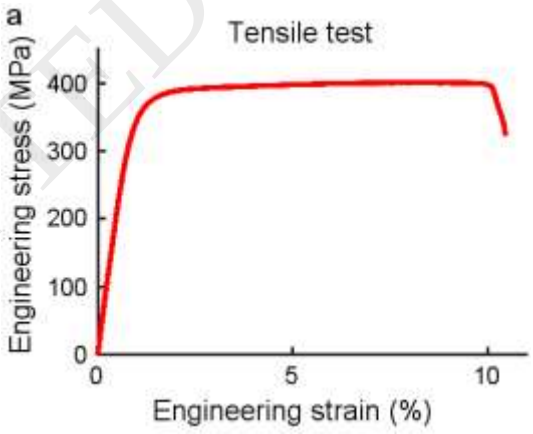

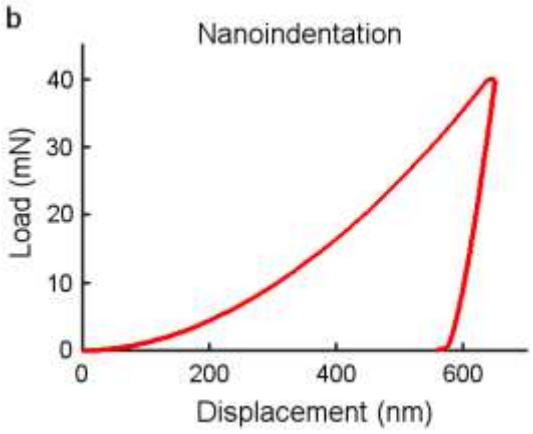

Fig. 7. Mechanical testing: (a) stress-strain curve from tensile test to find yield stress, and (b) load-displacement curve from nanoindentation test to find Young's modulus.

3. Theory and calculations

Consider an internal channel of breadth *b* (extending into the plane of the paper) whose upper half is in the process of being built using PBF, where layer *j* was the last to be added and the total number of layers before the right and left halves of the channel meet is *n*, as shown in Fig. 8a. The shape of the overhang is described by the positions of the discrete nodes (labeled 1 to *n* in Fig. 8a) whose X and Y displacements (*w* and *v*, respectively) are sought in order to calculate the shape deviation of the channel. The overhang is assumed to be a cantilever beam (Fig. 8b) that obeys the Euler-Bernoulli beam theory; this assumption is justified because the deformations arising out of the PBF process are typically much smaller compared to the part dimensions, so that all the planes of the cantilever beam (Fig. 8b) perpendicular to the beam's neutral axis can be assumed to remain perpendicular to the neutral axis after deflection, which is a key requirement of the theory [55]. It should be noted that the left side of the cantilever in Fig. 8b can be assumed to be clamped (i.e. zero displacement and zero slope) due to the large distance (10 mm) of the edge of the channels from the edge of the coupon (Figs. 5a-c). The thickness of this cantilever varies along the X-direction and this variation, *h(x)*, depends upon the shape of the channel; expressions of *h(x)*

for the three different channel shapes considered in this study (circular, elliptical, and diamond-shaped) after the deposition of layer *j* are given in Table 3.

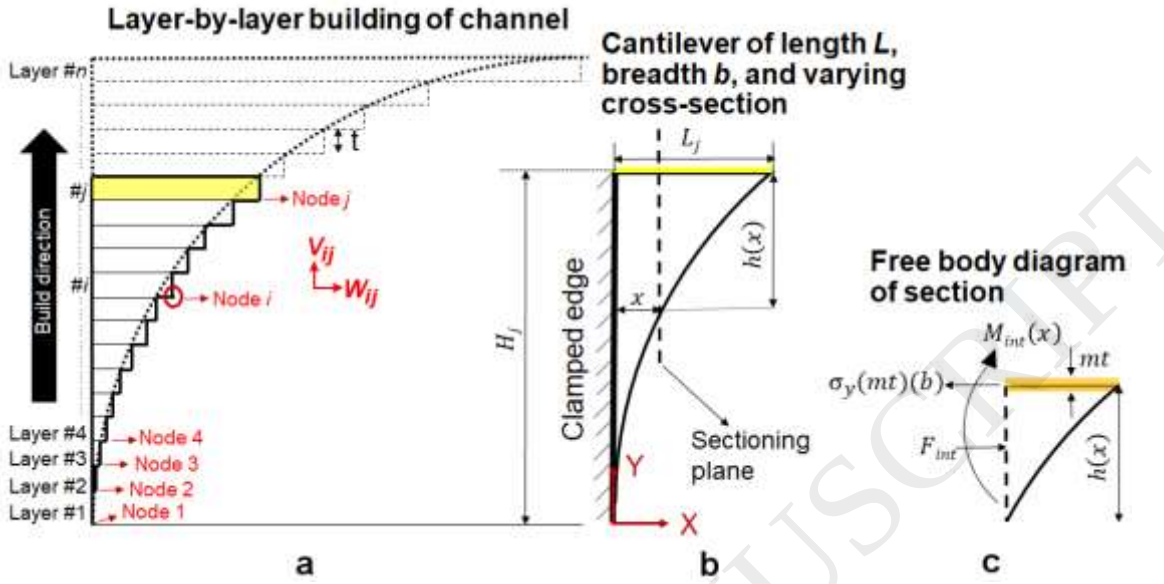

Fig. 8. Model schematic: (a) one half of circular channel in the process of being built up using PBF where the last layer to be fused was layer #*j*, (b) modeling the overhanging region up to layer #*j* as a cantilever of varying cross-sectional thickness *h(x)* depending upon the shape of the internal channel, and (c) free body diagram of a section of the cantilever at a distance *x* from the origin. The build direction is along the Y-axis.

Table 3
Expressions for *h(x)* for different channel shapes after deposition of layer *j*.

Shape	*h(x)* =	Explanation of terms
Circular	$H_j - \sqrt{2Rx - x^2}$	R = radius of circle, $H_j = jt$
Elliptical	$H_j - \frac{b}{a}\sqrt{2ax - x^2}$	a = half of major axis (along X-direction), b = half of minor axis (along Y-direction), $H_j = jt$
Diamond	$H_j - x\cot\emptyset$	$\emptyset$ = angle w.r.t the build direction (i.e. Y-axis), $H_j = jt$

When the last layer *j* solidifies and is not allowed to contract by the solidified material beneath it, a tensile residual stress develops in the melted layer(s) that can be assumed to be equal to the yield stress (σ_y) of the material [18,26,56]; moreover, since the melt pool depth is usually more than one layer thickness (t) to ensure complete adherence of the deposited layer and high part densities, the thickness of the layer carrying a tensile residual stress of σ_y is

equal to *mt*, where *m* is defined as the ratio of melt penetration depth to the layer thickness. Taking a section of the cantilever located at a distance *x* from the origin and drawing the free body diagram of the free end of the section (Fig. 8c), the resulting internal forces and moments can thus be obtained from force and moment balance:

$$F_{int} = \sigma_y mtb \tag{1}$$

$$M_{int}(x) = \sigma_y mtb \frac{h(x)+t}{2} \tag{2}$$

$F_{int}(x)$ is the internal normal force that causes compression of the cantilever, while $M_{int}(x)$ is the internal moment that causes upward (concave) bending of the cantilever, both of which contribute to the shape deviation of the internal channel by causing deformations along the -X and +Y directions, respectively.

3.1 Shape deviation due to axial compression

The deformation, $\delta(x)$, due to axial compression of a cantilever of variable cross-sectional area is given by [57]:

$$\delta(x) = -\frac{F_{int}}{E}\int_0^x \frac{dx}{A(x)} = -\frac{\sigma_y mt}{E}\int_0^x \frac{dx}{h(x)+t} \tag{3}$$

where the variable cross-sectional area, $A(x)$, is equal to $b\times(h(x)+t)$, and F_{int} is obtained from Eq. 1. In general, the X-displacement of any given node i ($1 \le i \le n$) due to layer j ($i \le j \le n$) is:

$$w_{ij} = \delta(x_i) = -\frac{\sigma_y mt}{E}\int_0^{x_i} \frac{dx}{h(x)+t} \tag{4}$$

where x_i is the X-coordinate of node i and $h(x)$ is given in Table 3. Due to the cumulative nature of deformation in the PBF process, whereby the deflection of a given node i will be affected by all the layers deposited during and after layer i, the final X-displacement of node i is:

$$w_i = \sum_{j=i}^{n} w_{ij} \tag{5}$$

3.2 Shape deviation due to bending

To calculate the vertical displacement ($\Delta(x)$) due to bending, the moment-curvature relationship for an Euler-Bernoulli beam [57] is invoked:

$$\frac{M_{int}(x)}{EI(x)} = \frac{d^2\Delta}{dx^2} \tag{6}$$

Also, since the bending cross-section is rectangular:

$$I(x) = \frac{1}{12} b[h(x) + t]^3 \tag{7}$$

From Eqs. 2, 6 and 7:

$$\frac{d^2\Delta}{dx^2} = \frac{6\sigma_y mt}{E} \frac{1}{[h(x)+t]^2} \tag{8}$$

Eq. 8 is a second-order ordinary differential equation (ODE) in which $\Delta(x)$ can be solved using the following initial conditions:

$$\Delta = 0 \;\; at \; x = 0 \tag{9a}$$

$$\frac{d\Delta}{dx} = 0 \;\; at \; x = 0 \tag{9b}$$

The vertical bending displacement of node *i* due to deposition of layer *j* is calculated by seeking the solution of $\Delta(x)$ (from Eqs. 8 and 9 where $h(x)$ is given in Table 3) at the X-coordinate of node *i*:

$$v_{ij} = \Delta(x_i) \tag{10}$$

Moreover, similar to the axial deformation case, the cumulative nature of the PBF process means that the final bending displacement of node *i* is given by:

$$v_i = \sum_{j=i}^{n} v_{ij} \tag{11}$$

Eqs. 4-5 and 8-11 are sufficient to calculate node displacements due to axial and bending deformations of a cantilever beam of any desired shape; however, the ODE system of Eqs. 8-9 does not have a closed-form solution for the circular and elliptical functional forms of $h(x)$ given in Table 3. Consequently, the ODE was numerically solved using the 'ode45' [58] subroutine of MATLAB for the circular and elliptical profiles, while the diamond-shaped

profile permitted an analytical solution as described in Section 3.3. It should be noted that the above analysis is only valid till layer *n*-1 i.e. till the left and right halves of the channel's overhanging regions do not meet; once the bridge is formed by the deposition of layer *n*, the cantilever model ceases to be valid.

3.3 Analytical solution for deformation of diamond-shaped channel

Substituting the expression for $h(x)$ for a diamond-shaped channel from Table 3 into Eq. 4:

$$w_{ij} = -\frac{\sigma_y m t}{E}\int_0^{x_i}\frac{dx}{H_j+t-x\cot\emptyset} = -\frac{\sigma_y m t\tan\emptyset}{E}\log\left|\frac{H_j+t}{H_j+t-x_i\cot\emptyset}\right| \quad (12)$$

Recognizing that $x_{j+1} = (H_j + t)\tan\emptyset$ for a diamond-shaped channel and defining a non-dimensional coordinate, x_{ij}^*:

$$x_{ij}^* = \frac{x_i}{x_{j+1}} \quad (13)$$

leads to:

$$w_{ij} = -\frac{\sigma_y m t\tan\emptyset}{E}\log\left|\frac{1}{1-x_{ij}^*}\right| \quad (14)$$

The definition of x_{ij}^* in Eq. 13 ensures that its highest value is $\frac{x_i}{x_{j+1}} < 1$, thus avoiding a mathematical singularity in Eq. 14; physically, this means that the discrete layer-by-layer nature of the PBF process (e.g. Fig. 8a) is taken into account where the cantilever thickness at node *j* is equal to the layer thickness (t) as opposed to the idealized cantilever model (e.g. Fig. 8b) where the thickness at this node would have been zero.

To solve the ODE system represented by Eqs. 8-9 for the bending deformation, the expression for $h(x)$ for a diamond-shaped channel from Table 3 is substituted into Eq. 8. Integrating once:

$$\frac{d\Delta}{dx} = \frac{6\sigma_y m t}{E}\int\frac{1}{[H_j+t-x\cot\emptyset]^2}dx + C_1 = \frac{6\sigma_y m t\tan\emptyset}{E}\frac{1}{(H_j+t-x\cot\emptyset)} + C_1 \quad (15)$$

Using the initial condition given by Eq. 9b in Eq. 15:

$$\frac{d\Delta}{dx} = \frac{6\sigma_y mt \tan\emptyset}{E}\left[\frac{1}{(H_j+t-x\cot\emptyset)} - \frac{1}{(H_j+t)}\right] \quad (16)$$

Integrating again and using the initial condition given by Eq. 9a:

$$\Delta(x) = \frac{6\sigma_y mt \tan^2\emptyset}{E}\left[\log\left|\frac{H_j+t}{H_j+t-x\cot\emptyset}\right| - \frac{x\cot\emptyset}{(H_j+t)}\right] \quad (17)$$

Using the same definition of x_{ij}^* given in Eq. 13, Eq. 17 can be rewritten for the bending deformation of node *i* as:

$$v_{ij} = \frac{6\sigma_y mt \tan^2\emptyset}{E}\left[\log\left|\frac{1}{1-x_{ij}^*}\right| - x_{ij}^*\right] \quad (18)$$

w_{ij} and v_{ij} represent the axial and bending deformations of node *i* ($1 \leq i \leq n$) due to deposition of layer *j* ($i \leq j \leq n$); the summation given by Eqs. 5 and 11 is then carried out (using MATLAB) to get the final deformation profile of the diamond-shaped channel.

4. Results and discussion

4.1 Mechanical properties as model inputs

The analytical method described in Section 3 can be used to predict the axial and bending deformation of overhanging regions in internal channels with prior knowledge of material properties, namely, yield stress (σ_y), Young's modulus (E), and melt depth-to-layer thickness ratio (*m*). The values for the above properties pertaining to as-built 17-4 PH stainless steel used in this work are given in Table 4. The measured properties were in good agreement with the reported values for the yield stress [59,60] and Young's modulus [61] of 17-4 PH stainless steel. In the PBF process, the processing parameters (mainly laser power, hatch spacing and scan speed for a given layer thickness) are experimentally optimized to minimize part porosity and maximize build speed; the optimal laser power and scan speed in conjunction with the thermal properties of the material (thermal conductivity, specific heat, and density) then determine the melt depth from which *m* can be calculated. The measurement of *m* entails conducting single laser track experiments which was outside the

scope of this study; hence, literature values of melt pool depths for 316L stainless steel (167 μm from Keller *et al*. [36] and 140 μm from Kamath *et al*. [62], both for a layer thickness of 30 μm), utilizing the same processing parameters as this study (200 W laser power, 800 mm/s scan speed), were used to calculate *m*, which was subsequently set as equal to 5.17. It must be noted that the minimum value of *m* to ensure complete adhesion of the newly deposited layer with the previously deposited layers is 2, which is less than the value chosen for this study.

Table 4
Material properties used in the analytical model.

Property	Value	Source
Yield stress (σ_y)	679 ± 5 MPa	Tensile test (this work)
Young's modulus (*E*)	209 ± 11 GPa	Nanoindentation (this work)
Melt depth/layer thickness (*m*)	5.17	Kamath *et al*. [62], Keller *et al*. [36] (for 316L stainless steel)

4.2 Prediction of shape deviation in internal channels

4.2.1 Circular channels

The deformation predictions (w_{ij} and v_{ij}) from the model described in Sections 3.1 and 3.2 were added to the designed profile (along the X and Y-directions, respectively) and plotted with the actual xy-coordinates of channels, as shown in Figs. 9a-c. As expected, the observed shape deviation was more prominent at higher polar angles due to the longer local overhangs encountered at higher angles. It is evident that the model was able to capture this trend and showed very good agreement with the residual stress-induced shape deviation of the circular channels for all the three radii.

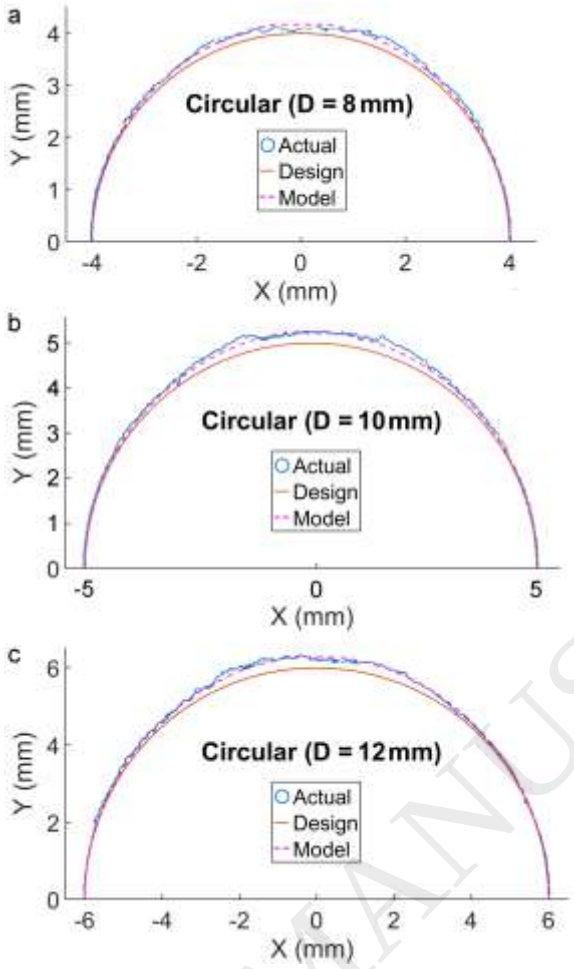

Fig. 9. Shape deviation (top half) for circular channels of diameter: (a) 8 mm, (b) 10 mm, and (c) 12 mm.

Fig. 10a further shows the total deformation ($\sqrt{w_i^2 + v_i^2}$) of each node *i* against the polar angle θ for the circular channel – this plot can be used to identify the demarcation between Regions II and III (defined by Wang *et al*. [41] and shown in Fig. 2a) and determine the critical polar angle from where a redesign to a teardrop shape (or other preventive measures) can be implemented. It is seen that there is a sudden jump in the deformation at θ ~ 85° representing the last layer that is deposited; since the last layer acts as a bridge between the right and left halves of the channel as discussed at the end of Section 3.2, the cantilever model prediction for the deformation of the final node is not valid and is neglected in Figs. 9a-c. Although the final deposited layer does not induce cantilever bending, the melt pool penetration due to laser scanning over loose powder caused a minor dip due to dross

formation at the top of the channels, as seen in Figs. 9a-c. Interestingly, the deflection-θ plots of Fig. 10a, when normalized by the respective radii, collapsed into a single curve as shown in Fig. 10b. This indicates that, for instance, the expected deviation at θ = 75° will always be around 4.5 % of the radius irrespective of the radius of the circle; although this particular relation only holds for the material under consideration here (17-4 PH stainless steel), it is a trivial task to develop such design relations for other PBF materials with prior knowledge of the respective material properties.

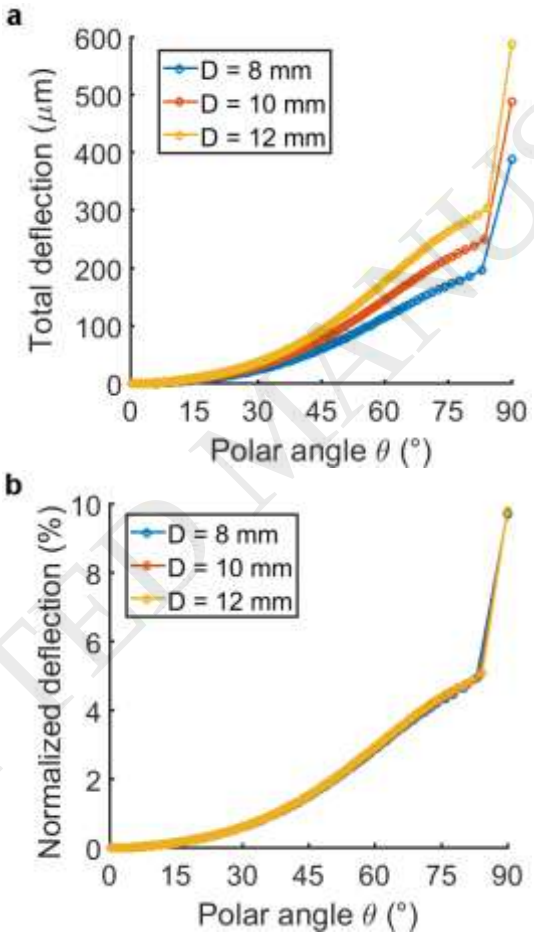

Fig. 10. Model prediction of deflection for three different circular cases as a function of polar angle: (a) total deflection ($\sqrt{w_i^2 + v_i^2}$), and (b) deflection normalized by radius ($\frac{\sqrt{w_i^2 + v_i^2}}{R}$).

4.2.2 Elliptical channels

The channel profiles along with the model predictions for elliptical channels of three different (vertical) minor axes are shown in Figs. 11a-c. It must be noted that these elliptical profiles have long overhanging regions at the top and are not expected to be built in this configuration in real applications; however, they were chosen to test the model's prediction capabilities for severe overhangs. It is seen from Figs. 11a-c that the model over-predicted the shape deviation near the top of the channels (where dross formation caused a significant dip in the channel profile) but agreed well with the channel profiles elsewhere.

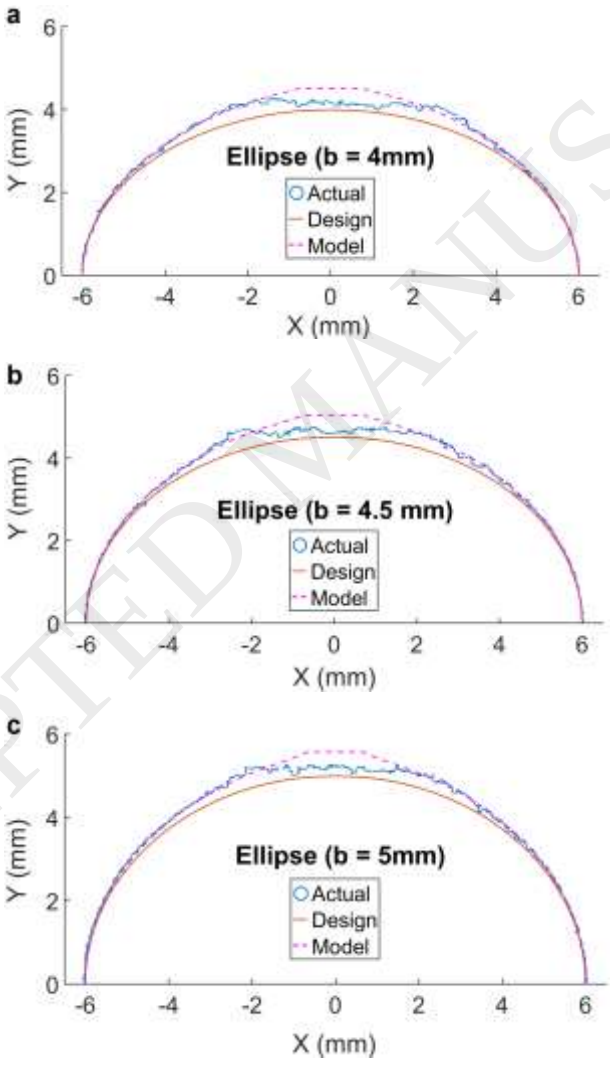

Fig. 11. Shape deviation (top half) for elliptical channels of half-minor axis: (a) 4 mm, (b) 4.5 mm, and (c) 5 mm.

4.2.3 Diamond-shaped channels

The experimental results and model predictions for diamond-shaped channels are shown in Figs. 12a-c; as mentioned earlier, this was the only cross-sectional shape that permitted a closed-form solution given by Eqs. 14 and 18. Unlike the circular and elliptical cases, the diamond shape has local overhangs of equal length (equal to $t \times \tan Ø$) through its entire height. Both the axial and bending deformations are seen to be a function of the overhang angle Ø, the former being proportional to tan Ø while the latter being proportional to $\tan^2 Ø$. This dependence is clearly seen in Figs. 12a-c, where the predicted maximum deflection nearly doubled from ~160 µm for Ø = 40° to ~316 µm for Ø = 50° ($[\frac{\tan 50}{\tan 40}]^2 \sim 2$).

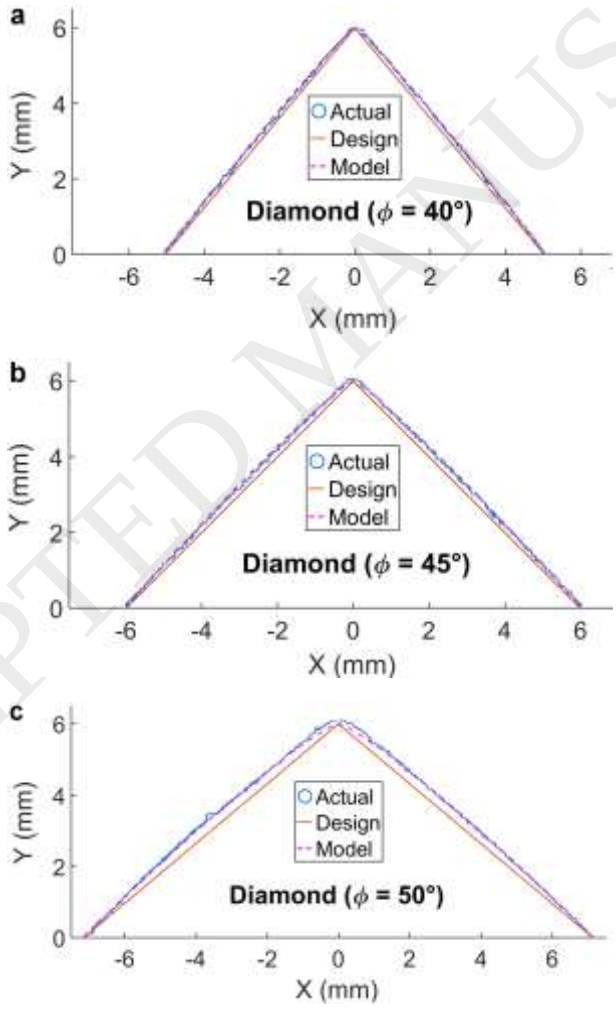

Fig. 12. Shape deviation (top half) for diamond-shaped channels of angle Ø with respect to vertical of: (a) 40°, (b) 45°, and (c) 50°.

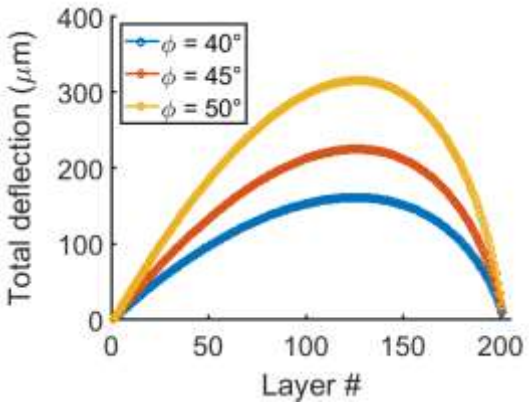

Fig. 13. Model prediction of total deflection ($\sqrt{w_i^2 + v_i^2}$) for three different diamond-shaped channels as a function of deposited layers.

The fact that the function $\tan^2 Ø$ increases rapidly for Ø > 45° can also explain why an angle of 45° with respect to the vertical is often cited as a 'critical' angle for overhanging regions [39,41] as a design rule-of-thumb. Interestingly, 'concaving' of the linear portion of the diamond-shaped profiles was observed (seen most clearly for Ø=50° in Fig. 12c) where the maximum deflection occurred around layer #125 out of a total of 200 layers as shown in Fig. 13; this concaving effect was also visible in the triangular holes built by Thomas [39] using PBF, although it wasn't identified as such by the author. This phenomenon can be explained as follows:

1) From Eqs. 14 and 18, it is seen that the deformation of a given node *i* due to the deposition of layer *j* depends upon $\log|\frac{1}{1-x_{ij}^*}| - x_{ij}^*$, where $x_{ij}^* = x_i/x_{j+1}$ is the non-dimensional X-coordinate of the i^{th} node normalized by the cantilever length after the deposition of layer *j*+1. Higher values of x_{ij}^* are caused by higher values of *i*; in other words, the later the layer *i* is deposited, the higher will be the deformations of node *i* caused by subsequent layers equal to or greater than *i*. Physically, this simply means that the deflections of nodes increase the further away from the clamped edge they are, which makes intuitive sense.

2) Due to the cumulative nature of deflection encountered in the PBF process (Eqs. 5 and 11), the deformation of a given node *i* also depends upon how many layers are deposited after it and thus affect it.

It is now evident why the maximum displacement is observed to be in the middle (Fig. 13): this is because the middle nodes are far enough away from the clamped edge to have high deflections (point 1), and are situated low enough compared to the total cantilever height to have enough layers deposited after them adding to their deflections (point 2). Finally, it must be noted that the deflection plots of Fig. 13 are only valid for the chosen height (6 mm) of the upper half of the channels, and that the maximum deflections are expected to increase with an increase of channel height (i.e. the number of deposited layers).

4.3 Effect of material properties and processing parameters

The axial and bending deformation of internal channels depends, in general, upon the factor $\frac{\sigma_y m}{E}$, which can be a useful tool for material and processing parameter selection. For instance, consider the alloys Ti-6Al-4V and Al-Si10-Mg, both of which are popular choices for the PBF process. σ_y, E, and the ratio σ_y/E of both alloys are given in Table 5, where the material properties were obtained from EOS [63], a popular laser PBF machine supplier. The ratios indicate that Ti-6Al-4V should have a greater tendency for deformation compared to Al-Si10-Mg (about three times greater assuming similar values *m* values for both) -- this was experimentally observed by Calignano [44] who reported that overhangs made from the titanium alloy were more susceptible to distortion and build failure than the aluminum alloy. Thus, the model can aid the designer in comparing and choosing materials to ensure minimal warpage during the PBF build process.

Table 5
Material properties for two popular PBF alloys.

Property	Ti-6Al-6V	Al-Si10-Mg
Yield stress (σ_y, MPa)	1125	220
Young's modulus (E, GPa)	108	70
σ_y/E	10.4×10^{-3}	3.14×10^{-3}

The ratio m is a function of processing parameters and is usually the result of experimental studies on density optimization. It can be envisioned that shape deviation can be significantly reduced by adjusting the processing parameters to reduce the melt pool depth and, consequently, m; however, this is likely to occur at the cost of introducing lack-of-fusion porosity into the part. A processing challenge could thus be to find the optimal set of parameters (laser power, scan speed, and hatch spacing) that can achieve high densities at the lowest possible melt depths, especially for applications that have strict restrictions upon warpage of overhangs or shape deviation of internal channels.

4.4 Pre-print shape compensation

Since overhanging regions warp up during PBF processing, a potential approach towards reducing shape deviation in internal channels is to compensate for the expected warpage during the design stage, so that the PBF-built part can adhere to the desired shape. This is achieved by subtracting the axial and bending deformations (Eqs. 5 and 11) from the designed shape so that deformations during the PBF process can bring the shape back up to the desired profile. Figs. 14a-c show the results for three circular channels (D = 12 mm): a vertically built channel, a horizontally built channel with shape compensation, and a horizontally built channel with no shape compensation, respectively. It is evident that the shape compensation strategy was successful in reducing the shape deviation of the horizontally built channel (Fig. 14b) when compared to the sample with no compensation

(Fig. 14a). The root mean square (RMS) deviation from the target of the above channels was calculated as:

$$RMS_{dev} = \sqrt{\frac{\sum_{i=1}^{n}(r_{actual,i} - R_{target})^2}{n}} \quad (19)$$

where $r_{actual,i}$ is the radial coordinate of a given point in the top half of the channel, R_{target} is the desired radius of the circle (6 mm in this case), and n is the total number of points (obtained from image processing) in the top half. It can be seen from Table 6 that the shape compensation strategy reduced the RMS deviation by a factor of 2, from 100 μm to 52 μm. Although the residual stress-induced deformation was accounted for, the roughness due to dross formation at the top still affected the RMS after shape compensation; the lowest possible RMS deviation (19 μm) was observed in the vertically built channel with no overhangs (Fig. 14c) where the roughness and residual stress-induced deviations were the minimum.

Table 6
RMS deviation due to shape compensation.

	Horizontal		Vertical
	No compensation	With compensation	
RMS deviation of top half (μm)	100	52	19

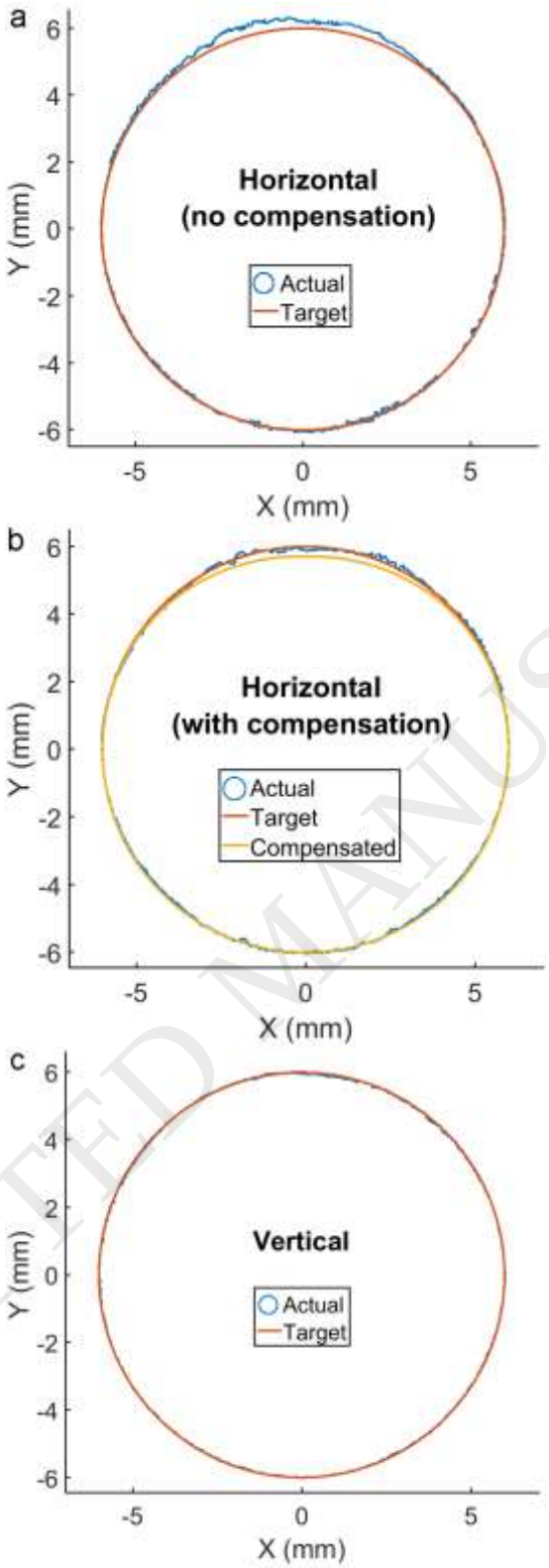

Fig. 14. Pre-print shape compensation for circular channel: (a) horizontally built with no compensation, (b) horizontally built with compensation, and (c) vertically built (reference case).

5. Conclusions

(1) In this work, an analytical tool was developed to predict the shape deviation of overhanging regions in internal channels built using the PBF process. Treating the overhanging region as a cantilever of varying thickness loaded by the tensile residual stress in the melted layers at the top, the method used classical Euler-Bernoulli beam theory to calculate the axial and bending deformation of the overhanging regions of internal channels to predict the shape deviation from the designed profile. The material properties for 17-4 PH stainless steel required as inputs for the model were measured through tensile and nanoindentation tests.

(2) The predicted shape deviation showed very good agreement with the experimentally obtained profiles of channels of three different cross-sections (circular, elliptical, and diamond-shaped); moreover, the derived differential equations (Eqs. 4, 5, 8-11) are simple and general enough to be applied to any desired overhang or channel shape to predict its shape deviation.

(3) A closed-form solution was obtained for the shape deviation of the diamond-shaped profile (Eq. 18), which showed that the bending deformation was proportional to $\tan^2 Ø$, where Ø is the angle made by the linear portion of the diamond with respect to the build direction. This indicates that overhangs built with $Ø > 45°$ will have a greater propensity towards warpage, agreeing with previous experimental observations in the literature [39,41].

(4) Shape deviation was found to be proportional to the yield stress, the melt penetration depth, and the inverse of Young's modulus; this predicted dependence upon material properties agreed with experimental observations in the literature [44], suggesting that the model can be used by designers to make judicious material and/or processing parameter choices when fabricating overhanging regions with restrictions upon shape deviation.

(5) The model was further used to build a shape-compensated model where the expected deviations were subtracted from the desired profile in the design stage before the build; this shape compensation strategy was successful in reducing the RMS deviation of the top half of a circular channel by a factor of 2.

(6) Finally, the analytical method developed in this study is expected to be a useful tool for laser-based AM users by providing a mathematical framework to establish design-for-AM guidelines and compensation strategies for overhanging regions in internal channels, with the ultimate aim of reducing build failures and achieving tighter tolerances.

Acknowledgements

This research was carried out under project number S16044 in the framework of the Partnership Program of the Materials innovation institute M2i (www.m2i.nl) and the Technology Foundation STW (www.stw.nl), which is part of the Netherlands Organisation for Scientific Research (www.nwo.nl). The authors acknowledge valuable discussions with Dr. Thomas Pijper, Philips Personal Care, Drachten, the Netherlands.

References

[1] ASTM F2792 - Standard Terminology for Additive Manufacturing Technologies, 2013. doi:10.1520/F2792-12A.2.

[2] C.Y. Yap, C.K. Chua, Z.L. Dong, Z.H. Liu, D.Q. Zhang, L.E. Loh, S.L. Sing, Review of selective laser melting : Materials and applications, Appl. Phys. Rev. 2 (2015). doi:10.1063/1.4935926.

[3] N.T. Aboulkhair, N.M. Everitt, I. Ashcroft, C. Tuck, Reducing porosity in AlSi10Mg parts processed by selective laser melting, Addit. Manuf. 1 (2014) 77–86. doi:10.1016/j.addma.2014.08.001.

[4] B. Vandenbroucke, J.P. Kruth, Selective laser melting of biocompatible metals for rapid manufacturing of medical parts, Rapid Prototyp. J. 13 (2007) 196–203. doi:10.1108/13552540710776142.

[5] T. Debroy, H.L. Wei, J.S. Zuback, T. Mukherjee, J.W. Elmer, J.O. Milewski, A.M. Beese, A. Wilson-heid, A. De, W. Zhang, Additive manufacturing of metallic components – Process , structure and properties, Prog. Mater. Sci. 92 (2018) 112–224.

[6] H. Rotaru, R. Schumacher, S.-G. Kim, C. Dinu, Erratum to: Selective laser melted titanium implants: a new technique for the reconstruction of extensive zygomatic complex defects, Maxillofac. Plast. Reconstr. Surg. 37 (2015) 12. doi:10.1186/s40902-015-0012-6.

[7] C. Yan, L. Hao, A. Hussein, D. Raymont, Evaluations of cellular lattice structures manufactured using selective laser melting, Int. J. Mach. Tools Manuf. 62 (2012) 32–38. doi:10.1016/j.ijmachtools.2012.06.002.

[8] E. Hilpert, J. Hartung, S. Risse, R. Eberhardt, A. Tünnermann, Precision manufacturing of a lightweight mirror body made by selective laser melting, Precis. Eng. 53 (2018) 310–317. doi:10.1016/j.precisioneng.2018.04.013.

[9] C.-Y. Lin, T. Wirtz, F. LaMarca, S.J. Hollister, Structural and mechanical evaluations of a topology optimized titanium interbody fusion cage fabricated by selective laser melting process., J. Biomed. Mater. Res. A. 83 (2007) 272–279. doi:10.1002/jbm.a.31231.

[10] C. Emmelmann, P. Sander, J. Kranz, E. Wycisk, Laser additive manufacturing and bionics: Redefining lightweight design, Phys. Procedia. 12 (2011) 364–368. doi:10.1016/j.phpro.2011.03.046.

[11] K.L. Kirsch, K.A. Thole, Heat Transfer and Pressure Loss Measurements in Additively Manufactured Wavy Microchannels, J. Turbomach. 139 (2016) 11007–11009. http://dx.doi.org/10.1115/1.4034342.

[12] M. Mazur, P. Brincat, M. Leary, M. Brandt, Numerical and experimental evaluation of a conformally cooled H13 steel injection mould manufactured with selective laser melting, Int. J. Adv. Manuf. Technol. (2017) 1–20. doi:10.1007/s00170-017-0426-7.

[13] A. Armillotta, R. Baraggi, S. Fasoli, SLM tooling for die casting with conformal cooling channels, Int. J. Adv. Manuf. Technol. 71 (2014) 573–583. doi:10.1007/s00170-013-5523-7.

[14] D. Thomas, S. Gilbert, Costs and Cost Effectiveness of Additive Manufacturing: A Literature Review and Discussion, 2014. doi:10.6028/NIST.SP.1176.

[15] J.O. Milewski, Additive Manufacturing of Metals, 1st ed., Springer International Publishing, 2017. doi:10.1007/978-3-319-58205-4.

[16] EMPA, Selective Laser Melting, (n.d.). https://www.empa.ch/web/coating-competence-center/selective-laser-melting (accessed May 26, 2019).

[17] P.J. Withers, H.K.D.H. Bhadeshia, Residual stress. Part 1 – Measurement techniques, Mater. Sci. Technol. 17 (2001) 355–365. doi:10.1179/026708301101509980.

[18] P. Mercelis, J.P. Kruth, Residual stresses in selective laser sintering and selective laser melting, Rapid Prototyp. J. 12 (2006) 254–265. doi:10.1108/13552540610707013.

[19] W.J. Sames, F. a List, S. Pannala, R.R. Dehoff, S.S. Babu, The metallurgy and processing science of metal additive manufacturing, Int. Mater. Rev. 6608 (2016) 1–46. doi:10.1080/09506608.2015.1116649.

[20] B. Vrancken, Study of Residual Stresses in Selective Laser Melting, KU Leuven, 2016. https://lirias.kuleuven.be/bitstream/123456789/542751/1/thesis+Bey+Vrancken+v01-06-2016+FINAL_compressed.pdf.

[21] L. Kempen, L. Thijs, B. Vrancken, S. Buls, J. Van Humbeeck, J.-P. Kruth, Producing crack-free, high density M2 HSS parts by Selective Laser Melting: Pre-heating the baseplate, in: Proc. 24th Int. Solid Free. Fabr. Symp., Austin, TX, 2013: pp. 131–139.

[22] T. Craeghs, S. Clijsters, E. Yasa, J.-P. Kruth, Online quality control of selective laser melting, in: Proc. 22nd Int. Solid Free. Fabr. Symp., Austin, TX, 2011: pp. 212–226. doi:10.1080/01402390.2011.569130.

[23] S. Afazov, A. Okioga, A. Holloway, W. Denmark, A. Triantaphyllou, S.A. Smith, L. Bradley-Smith, A methodology for precision additive manufacturing through compensation, Precis. Eng. 50 (2017) 269–274. doi:10.1016/j.precisioneng.2017.05.014.

[24] M. Matsumoto, M. Shiomi, K. Osakada, F. Abe, Finite element analysis of single layer forming on metallic powder bed in rapid prototyping by selective laser processing, Int. J. Mach. Tools Manuf. 42 (2002) 61–67. doi:10.1016/S0890-6955(01)00093-1.

[25] N.W. Klingbeil, J.L. Beuth, R.K. Chin, C.H. Amon, Residual stress-induced warping in direct metal solid freeform fabrication, Int. J. Mech. Sci. 44 (2002) 57–77. doi:10.1016/S0020-7403(01)00084-4.

[26] M. Shiomi, K. Osakada, K. Nakamura, T. Yamashita, F. Abe, Residual stress within metallic model made by selective laser melting process, CIRP Ann. - Manuf. Technol. 53 (2004) 195–198. doi:10.1016/S0007-8506(07)60677-5.

[27] O. Fergani, F. Berto, T. Welo, S.Y. Liang, Analytical modelling of residual stress in additive manufacturing, Fatigue Fract. Eng. Mater. Struct. 40 (2017) 971–978. doi:10.1111/ffe.12560.

[28] I.A. Roberts, Investigation of residual stresses in the laser melting of metal powders in additive layer manufacturing, University of Wolverhampton, 2012. https://wlv.openrepository.com/handle/2436/254913.

[29] B. Cheng, S. Shrestha, K. Chou, Stress and deformation evaluations of scanning strategy effect in selective laser melting, Addit. Manuf. 12 (2016) 240–251. doi:10.1016/j.addma.2016.05.007.

[30] L. Parry, I.A. Ashcroft, R.D. Wildman, Understanding the effect of laser scan strategy on residual stress in selective laser melting through thermo-mechanical simulation, Addit. Manuf. 12 (2016) 1–15. doi:10.1016/j.addma.2016.05.014.

[31] L. Wang, X. Jiang, Y. Zhu, X. Zhu, J. Sun, B. Yan, An approach to predict the residual stress and distortion during the selective laser melting of AlSi10Mg parts, Int. J. Adv. Manuf. Technol. 97 (2018) 3535–3546. doi:10.1007/s00170-018-2207-3.

[32] M.F. Zaeh, G. Branner, Investigations on residual stresses and deformations in selective laser

melting, Prod. Eng. 4 (2010) 35–45. doi:10.1007/s11740-009-0192-y.

[33] L. Papadakis, A. Loizou, J. Risse, J. Schrage, Numerical computation of component shape distortion manufactured by Selective Laser Melting, in: Int. Conf. Manuf. Light. Components - ManuLight 2014, 2014: pp. 90–95. doi:10.1016/j.procir.2014.06.113.

[34] C. Li, C.H. Fu, Y.B. Guo, F.Z. Fang, Fast Prediction and Validation of Part Distortion in Selective Laser Melting, Procedia Manuf. 1 (2015) 355–365. doi:10.1016/j.promfg.2015.09.042.

[35] C. Li, J.F. Liu, Y.B. Guo, Prediction of Residual Stress and Part Distortion in Selective Laser Melting, Procedia CIRP. 45 (2016) 171–174. doi:10.1016/j.procir.2016.02.058.

[36] N. Keller, V. Ploshikhin, New Method for Fast Predictions of Residual Stress and Distortions of AM Parts, in: Solid Free. Fabr. Symp., Austin, USA, 2014: pp. 1229–1237.

[37] S. Afazov, W.A.D. Denmark, B. Lazaro Toralles, A. Holloway, A. Yaghi, Distortion prediction and compensation in selective laser melting, Addit. Manuf. 17 (2017) 15–22. doi:10.1016/j.addma.2017.07.005.

[38] A.E. Patterson, S.L. Messimer, P.A. Farrington, Overhanging Features and the SLM/DMLS Residual Stresses Problem: Review and Future Research Need, Technologies. 5 (2017) 15. doi:10.3390/technologies5020015.

[39] D. Thomas, The Development of Design Rules for Selective Laser Melting, University of Wales Institute, Cardiff, 2009. https://repository.cardiffmet.ac.uk/handle/10369/913.

[40] J. Kranz, D. Herzog, C. Emmelmann, Design guidelines for laser additive manufacturing of lightweight structures in TiAl6V4, J. Laser Appl. 27 (2015) S14001. doi:10.2351/1.4885235.

[41] D. Wang, Y. Yang, Z. Yi, X. Su, Research on the fabricating quality optimization of the overhanging surface in SLM process, Int. J. Adv. Manuf. Technol. 65 (2013) 1471–1484. doi:10.1007/s00170-012-4271-4.

[42] D. Wang, S. Mai, D. Xiao, Y. Yang, Surface quality of the curved overhanging structure manufactured from 316-L stainless steel by SLM, Int. J. Adv. Manuf. Technol. 86 (2016) 781–792. doi:10.1007/s00170-015-8216-6.

[43] B. Cheng, K. Chou, Thermal Stresses Associated with Part Overhang Geometry in Electron Beam Additive Manufacturing: Process Parameter Effects, in: Solid Free. Fabr. Symp., Austin, USA, 2013: pp. 1076–1087.

[44] F. Calignano, Design optimization of supports for overhanging structures in aluminum and titanium alloys by selective laser melting, Mater. Des. 64 (2014) 203–213. doi:10.1016/j.matdes.2014.07.043.

[45] R. Mertens, S. Clijsters, K. Kempen, J.-P. Kruth, Optimization of Scan Strategies in Selective Laser Melting of Aluminum Parts With Downfacing Areas, J. Manuf. Sci. Eng. 136 (2014) 61012–61017. doi:10.1115/1.4028620.

[46] J. Pakkanen, F. Calignano, F. Trevisan, M. Lorusso, E.P. Ambrosio, D. Manfredi, P. Fino, Study of Internal Channel Surface Roughnesses Manufactured by Selective Laser Melting in Aluminum and Titanium Alloys, Metall. Mater. Trans. A Phys. Metall. Mater. Sci. 47 (2016) 1–8. doi:10.1007/s11661-016-3478-7.

[47] K. Kempen, F. Welkenhuyzen, J. Qian, J. Kruth, Dimensional accuracy of internal channels in SLM produced parts, in: Proc. Dimens. Accuracy Surf. Finish Addit. Manuf. ASPE Spring Top. Meet., 2014: pp. 76–79.

[48] S. Vock, B. Klöden, A. Kirchner, T. Weißgärber, B. Kieback, Powders for powder bed fusion: a review, Prog. Addit. Manuf. (2019). doi:10.1007/s40964-019-00078-6.

[49] B. Reinarz, J.T. Sehrt, G. Witt, O. Deiss, J. Van Kampen, J. Münzer, M. Ott, Optimization of media feed channels in Laser Beam Melting, in: Proc. Dimens. Accuracy Surf. Finish Addit. Manuf. ASPE Spring Top. Meet., 2014: pp. 13–18.

[50] J.C. Snyder, C.K. Stimpson, K.A. Thole, D.J. Mongillo, Build Direction Effects on Microchannel Tolerance and Surface Roughness, J. Mech. Des. 137 (2015) 111411. doi:10.1115/1.4031071.

[51] M. Mazur, M. Leary, M. Mcmillan, J. Elambasseril, M. Brandt, SLM additive manufacture of H13 tool steel with conformal cooling and structural lattices, Rapid Prototyp. J. 22 (2016) 504–518. doi:10.1108/RPJ-06-2014-0075.

[52] C.A. Schneider, W.S. Rasband, K.W. Eliceiri, NIH Image to ImageJ: 25 years of image analysis, Nat Meth. 9 (2012) 671–675. http://dx.doi.org/10.1038/nmeth.2089.

[53] Standard Test Methods for Tension Testing of Metallic Materials: E8/E8M - 16a, n.d. https://www.astm.org/DATABASE.CART/HISTORICAL/E8E8M-13.htm.

[54] A.C. Fischer-Cripps, Nanoindentation Testing, in: Nanoindentation. Mech. Eng. Ser., Springer, New York, NY, 2004: p. 282. doi:10.1007/978-1-4757-5943-3_2.

[55] O.A. Bauchau, J.I. Craig, Euler-Bernoulli beam theory, in: O.A. Bauchau, J.I. Craig (Eds.), Struct. Anal., Springer Netherlands, Dordrecht, 2009: pp. 173–221. doi:10.1007/978-90-481-2516-6_5.

[56] A.S. Wu, D.W. Brown, M. Kumar, G.F. Gallegos, W.E. King, An Experimental Investigation into Additive Manufacturing-Induced Residual Stresses in 316L Stainless Steel, Metall. Mater. Trans. A Phys. Metall. Mater. Sci. 45 (2014) 6260–6270. doi:10.1007/s11661-014-2549-x.

[57] S. Timoshenko, Strength of Materials: Part I Elementary Theory and Problems, 2nd ed., D. van Nostrant Company Inc., New York, NY, 1940.

[58] L.F. Shampine, M.W. Reichelt, The MATLAB ODE Suite, SIAM J. Sci. Comput. 18 (1997) 1–22. doi:10.1137/S1064827594276424.

[59] M. Mahmoudi, A. Elwany, A. Yadollahi, S.M. Thompson, L. Bian, N. Shamsaei, Mechanical properties and microstructural characterization of selective laser melted 17-4 PH stainless steel, Rapid Prototyp. J. 23 (2017) 280–294. doi:10.1108/RPJ-12-2015-0192.

[60] T. LeBrun, T. Nakamoto, K. Horikawa, H. Kobayashi, Effect of retained austenite on subsequent thermal processing and resultant mechanical properties of selective laser melted 17-4 PH stainless steel, Mater. Des. 81 (2015) 44–53. doi:10.1016/j.matdes.2015.05.026.

[61] M. Boiniardi, A. Casaroli, Stainless steels, Gruppo Lucefin, Esine, Italy, 2014.

[62] C. Kamath, B. El-Dasher, G.F. Gallegos, W.E. King, A. Sisto, Density of additively-manufactured, 316L SS parts using laser powder-bed fusion at powers up to 400 W, Int. J. Adv. Manuf. Technol. 74 (2014) 65–78. doi:10.1007/s00170-014-5954-9.

[63] EOS, Materials for Metal Additive Manufacturing, (n.d.). https://www.eos.info/material-m (accessed December 13, 2018).